

Enhanced weathering in the seabed: Rapid olivine dissolution and iron sulfide formation in submarine volcanic ash

WOLF-ACHIM KAHL^{1,2,*}, ANDREAS KLÜGEL¹, WOLFGANG BACH^{1,3}, AND M. MANGIR MURSHED^{2,4}

¹Department of Geosciences, University of Bremen, 28359 Bremen, Germany

²MAPEX Center for Materials and Processes, University of Bremen, 28334 Bremen, Germany

³MARUM Center for Marine Environmental Sciences, University of Bremen, 28359 Bremen, Germany

⁴Institute of Inorganic Chemistry and Crystallography, University of Bremen, 28359 Bremen, Germany

ABSTRACT

In basaltic volcanic ash recovered from a seamount at 3000 m water depth, we discovered marcasite and pyrite precipitation within cavities that formed by partial to complete dissolution of olivine. In places, these cavities are reminiscent of negative crystal shapes; elsewhere they apparently continue along cracks. In strong contrast, adjacent volcanic glass shows little, if any, evidence for dissolution. The FeS₂ precipitates were commonly found to be conjoined and planar aggregates, occurring in the center of the voids. Their maximum volume fraction in relation to the void space as determined by 2D and 3D imaging techniques corresponds to the amount of iron released by olivine dissolution. Almost all occurrences of FeS₂ precipitation are related to Cr-spinel inclusions in the former olivine. We propose that rapid olivine dissolution was initiated by reduced H₂S-bearing fluids at olivine grain boundaries or surfaces exposed by cracks. Many of these cracks are connected to spinel grains, where the iron liberated from olivine is mineralized as FeS₂, initially facilitated by heterogeneous nucleation. Subsequent pyrite and/or marcasite precipitation occurred as overgrowths on existing FeS₂ aggregates. The particular chemical environment of low-pH, hydrogen sulfide-bearing fluids may have enhanced olivine dissolution by (1) keeping Fe in solution and (2) sequestering important quantities of Fe as FeS₂. The in situ oxidation of ferrous Fe and precipitation of ferric hydroxides at the olivine surface commonly observed in oxic environments were obviously impeded. It would have slowed down olivine dissolution to rates more similar to the dissolution of basaltic glass. We have no direct indication that the process of rapid olivine dissolution was aided by seafloor life. However, the presence of fibrous structures with small sulfide particles could indicate late colonization of sulfate-reducing bacteria that may add an additional path of iron fixation.

Keywords: Olivine, pyrite, marcasite, seamount, Canary Islands, dissolution, alteration, X-ray microscopy

INTRODUCTION

Iron sulfide formation pathways are commonly linked to the degradation of organic matter (see Roberts 2015; and references therein). Examples include macroscopic iron sulfide nodules as remineralization of large-scale sedimentary organic matter fragments (Jiang et al. 2001) or microscopic iron sulfide aggregates formed by remineralization of organic matter within microfossil chambers (Passier et al. 1997; Roberts et al. 2005). In sulfidic environments, iron-bearing detrital minerals undergo drastic alteration (see a review of Roberts 2015): hydrogen sulfide, which in many near-surface geochemical environments is a byproduct of bacterial sulfate reduction or anaerobic oxidation of methane, reacts with Fe²⁺ released from detrital minerals by dissolution to form iron sulfide minerals (mackinawite, greigite, and pyrite). It is not uncommon for marcasite (FeS₂, orthorhombic) or pyrite (FeS₂, cubic) to replace greigite (Fe₃S₄, cubic) and mackinawite [(Fe,Ni)_{1+x}S (x = 0–0.07), tetragonal] when an excess of H₂S is present (Hunger and Benning 2007; Posfai et al. 1998; Roberts 2015).

To our knowledge, the presence of sulfides connected with the intense dissolution of olivine in a submarine volcanic setting

has not been described so far. It is unclear if this is a consequence of sparse sampling or of limited preservation of the appropriate boundary conditions for sulfide formation/conservation in this particular geological setting.

This communication seeks to unravel the formation of a striking reaction texture of FeS₂ within cavities in olivine phenocrysts, observed in glassy basaltic tephra from a seamount near the Canary Islands, Spain. While many of these cavities are reminiscent of the negative shapes of their crystal host, elsewhere these voids appear to continue and broaden along cracks. Notably, the delicate FeS₂ precipitates barely extend into the surrounding matrix of volcanic glass. We employ 2D and 3D spectroscopic methods to decipher mineral compositions and growth relations and thermodynamic/kinetic computations to elucidate potential conditions and mechanisms of this reaction texture. Finally, we assess whether a microbial contribution to this process of olivine dissolution and iron sulfide formation is essential at all.

GEOLOGICAL SETTING

The samples were recovered from Henry Seamount, a Cretaceous volcanic edifice 40 km southeast of El Hierro island, rising ~700 m above ~3700 m deep ocean floor (Fig. 1)

* E-mail: wakahl@uni-bremen.de. Orcid 0000-0003-3342-9893

(Gee et al. 2001; Klügel et al. 2011). The seamount was investigated and sampled during R/V Meteor cruises M66/1 and M146, which provided evidence for Pleistocene to present hydrothermal fluid circulation in the summit region. This evidence includes locally dense coverage by shells from vesicomyid clams, occurrence of authigenic barite, and localization of sites of weak fluid venting (Klügel et al. 2011, 2020). Most clams belong to the genus *Abyssogena southwardae*, which live in symbiosis with sulfide-oxidizing bacteria and are mostly buried in H₂S-rich sediment at hydrothermal vents and cold seeps (Krylova et al. 2010). Overall, the summit area of the seamount is variably covered by pelagic sediment.

Some samples from the top of the seamount contain heterolithic basaltic tephra and dispersed basaltic rock fragments, suggesting rejuvenated volcanic activity (Klügel et al. 2020). The tephra occurrences are commonly associated with clamshells. In addition, tephra from one sample released H₂S during recovery onboard. The samples investigated here represent the dominant lithology of an ash layer overlain by 10–13 cm of pelagic sediment, recovered by gravity coring at 3145 m water depth; similar observations were also made in ash samples from two other sites. A detailed description of this core (sample 22841-1) and the other samples is given in Klügel et al. (2018).

METHODS

Detailed fabric inspections of single fragments were performed on a field emission scanning electron microscope (SEM) Zeiss SUPRA 40 with a Bruker EDS-detector XFlash 6/30 operated at 15 kV. Mineral analyses and fabric inspections of polished thin sections of tephra samples were performed on a Cameca SX-100 electron probe microanalyzer (EPMA) at the Department of Geosciences, University of Bremen. Olivine was analyzed with 15 kV/30 nA, spinel with 15 kV/15 nA, and sulfide with 20 kV/20 nA, using a focused beam in all cases. Calibrations used natural minerals from the Smithsonian Institution (Jarosewich et al. 1980), in-house standards, and pure elements (Ni, Co); the built-in PAP correction was applied for data reduction. Analytical precision and accuracy were controlled by regular analyses of Smithsonian reference standards along

with the samples (see Table 1 for average olivine, spinel, and sulfide analyses and Online Materials' Table S1–S3 for individual analyses).

Raman spectra were collected at different locations of the polished section of sample 22841. The spectra were recorded on a LabRam ARAMIS (Horiba Jobin Yvon) Micro-Raman spectrometer equipped with a laser working at 633 nm and <20 mW output. The use of a 50× objective (Olympus) with a numerical aperture of 0.75 provides a focus spot of about 1 μm diameter when closing the confocal hole to 200 μm. By usage of a neutral density filter (setting D1, 90% reduction), the laser power on the sample surface was estimated to be about 0.33 mW. Raman spectra were collected in the range between 100 and 1000 cm⁻¹ with a spectral resolution of ~2 cm⁻¹ using a grating of 1800 grooves/mm and a thermoelectrically cooled CCD detector (Synapse, 1024 × 256 pixels). The Rayleigh position and the linearity of the spectrometer were calibrated against the silicon signal and the emission lines of a neon lamp, respectively.

For 3D X-ray microscopy (XRM), two particles (olivine single grain: sample 22841-1 A-SG; olivine multiple grains aggregate: 22841-1 A-MGA) were glued using nail polish onto the tip of a graphite pencil. Both particles were scanned in a 360° rotation conducted with the 3D X-ray microscope ZEISS Xradia 520 system of the MAPEX Center for Materials and Processes, University of Bremen, Germany. Particle 22841-1 A-SG was scanned in overview mode with 1.30 μm per voxel and a beam energy of 90 kV and an energy flux of 89 μA (and ZEISS filter LE3), and a smaller volume of interest (VOI) of this sample was scanned with 0.36 μm per voxel (90 kV, 89 μA, filter LE3). Particle 22841-1 A-MGA was scanned in overview mode with 2.44 μm per voxel (60 kV, 83 μA, filter LE3), and a smaller VOI was scanned with 0.78 μm per voxel (80 kV, 88 μA, filter LE3). Correction of ring artifacts and reconstruction of the spatial information on the linear attenuation coefficient in the samples was done using the ZEISS Reconstructor software. For each particle, an image volume of ca. 1000 × 1000 × 1000 voxels was available. All subsequent processing of volume data (e.g., rendering, filtering the raw data, segmentation, surface generation, 3D quantitative image analysis of iron sulfide volume fractions) was done using Avizo 2019 (FEI). For visualization of volume reconstructions and single slices, the Avizo filter module RekursiveExponential was used in 3D mode. For quantitative 3D image analyses of void and iron sulfide volumes, prior to segmentation and binarization, this step was followed by a non-local means filtering in 3D mode. Avizo module AmbientOcclusion was chosen to discriminate cavities inside volcanic ash particles from the surrounding region (Titschack et al. 2018). Avizo was also used to determine the volume fractions of iron sulfide in 2D electron microprobe BSE images.

In the reaction path modeling, volcanic glass, olivine, and organic carbon were reacted with seawater at 5 °C using Geochemist's Workbench 7.0 (Bethke 1996). The system had 1 kg of seawater, 10 g of glass, 2 g of olivine, and 0.1 g of organic carbon. This high water-to-rock ratio was chosen to reflect the porous

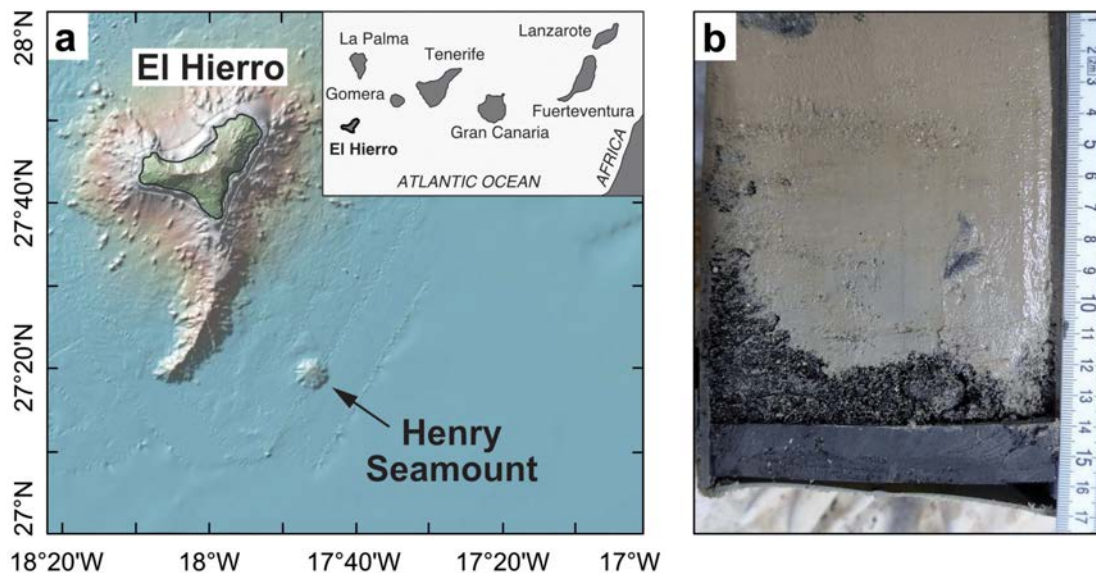


FIGURE 1. (a) Location map of El Hierro island and Henry Seamount, made with GeoMapApp (Ryan et al. 2009); inset shows the Canary Islands. (b) Gravity core sample GeoB22841-1 taken from the summit of the seamount. It contains coarse basaltic ash investigated here, overlain by marine sediment. (Color online.)

TABLE 1. Average olivine, spinel, and sulfide analyses of the investigated samples

Olivine (N = 33)											
wt%	SiO ₂	Al ₂ O ₃	FeO	MnO	MgO	CaO	NiO	Total	Fo%		
Average	39.33	0.05	17.68	0.26	43.64	0.32	0.23	101.6	81.5		
St.dev.	0.20	0.01	0.68	0.03	0.53	0.05	0.03	0.24	0.76		
Sulfide (N = 27)											
wt%	Mn	Fe	Ni	As	Cu	Co	Zn	Pb	Sb	S	Total
Average	0.939	43.66	0.535	0.049	0.007	0.016	0.042	0.178	0.010	52.64	98.07
St.dev.	0.450	0.46	0.118	0.021	0.013	0.014	0.019	0.069	0.015	0.65	0.80
Spinel (N = 19)											
wt%	MgO	CaO	TiO ₂	Cr ₂ O ₃	FeO _{tot}	MnO	SiO ₂	Al ₂ O ₃	Total	Cr#	Mg#
Average	10.077	0.041	4.383	24.421	38.567	0.297	0.080	17.684	95.547	48.30	45.04
St.dev.	0.811	0.037	1.120	1.714	3.299	0.039	0.034	2.595	0.737	2.45	3.85
afu per 3 cats.	Mg	Ti	Cr	Fe ³⁺	Fe ²⁺	Mn	Al	cations	O atoms		
Average	0.495	0.109	0.636	0.460	0.606	0.008	0.686	3.000	4.000		
St.dev.	0.030	0.030	0.034	0.056	0.059	0.001	0.088				

Note: See also Online Materials¹ Tables S1–S3 for individual analyses.

nature of the tephra layer in the shallow seabed. Graphite represents organic carbon, while fayalite represents olivine in the model. The reaction rates were assumed to be slowest for glass (10^{-16} mol cm⁻² s⁻¹), fastest for organic carbon (5×10^{-13} mol cm⁻² s⁻¹), and intermediate for olivine (10^{-15} mol cm⁻² s⁻¹). These rates reflect experimental constraints on the reaction rates of olivine and basaltic glass at neutral pH (Oelkers et al. 2018; Oelkers and Gislason 2001). We used rates lower than the ones measured at 25 °C to account for the lower temperature (5 °C). Empirical observations of breakdown rates of moderately old (100–1000 years) organic matter in seafloor sediments (Middelburg 1989) were used to approximate the graphite dissolution rate in the model. Thermodynamic data of minerals and aqueous species are from SUPCRT92 [Johnson et al. (1992) with updates from Wolery and Jove-Colon (2004)]. The thermodynamic properties of the volcanic glass were computed using a polyhedral approach for the average composition of sample 22841-1A (Klügel et al. 2020). Gibbs energies, entropies, volumes, and Maier-Kelly coefficients of the constituent oxides were taken from Helgeson et al. (1978) and updates in Wolery and Jove-Colon (2004). Equilibrium constants for dissolution reactions of the model glass composition were computed using aqueous species data from SUPCRT92 (Johnson et al. 1992) for a pressure of 25 MPa.

RESULTS

Petrography and microfabric on the grain scale

The ash particles investigated here consist of fresh glass of alkali basaltic composition with olivine phenocrysts (termed ash type 1 in Klügel et al. 2020). Olivine is euhedral to subhedral, up to 2 mm in size, and occurs isolated or in clusters. The crystals show a narrow compositional range of Fo_{79.5–82.6} (average Fo_{81.5}), 0.23–0.39 wt% CaO, 0.18–0.31 wt% NiO, and no systematic zonation (Table 1). They contain inclusions of spinel with Cr# = molar Cr/(Cr+Al) of 0.45–0.53, Mg# = molar Mg/(Mg+Fe²⁺) of 0.39–0.50, and Fe³⁺/Fe^{tot} of 0.40–0.45 (Table 1); occasional spinel microphenocrysts in the glass, and within iron sulfide precipitates, have similar compositions. By using the glass analyses in Klügel et al. (2020) and the Fe²⁺-Mg partition coefficient between olivine and melt after Toplis (2005), we obtain a melt Fe³⁺/Fe^{tot} ratio of 0.34.

Many olivine phenocrysts show pronounced development of iron sulfide within cavities inside the crystals (Figs. 2b and 2c). In places, these cavities are reminiscent of negative crystal shapes (Figs. 3a and 3b); elsewhere they apparently continue along cracks. Similar sulfide formation, albeit far less common and less intense, is found along cracks in some clinopyroxene phenocrysts in lithologically different ash fragments (Fig. 2a). Where cavities meet both olivine and host glass, SEM investigations revealed very limited dissolution features of the glass (Figs. 3b and 3c). In some cases, cavities clearly discernible @as

negative shapes of olivine crystals are entirely devoid of olivine material (Figs. 4a and 4c). Even in these cavities, iron sulfide precipitation does not appear to be irregular but organized in relation to initial cracks or microfissures in the former olivine host.

Microprobe analyses of the sulfides (Table 1) indicate FeS₂ stoichiometry with some Fe replaced by Ni (0.35–0.87 wt%) and Mn (0.39–1.84 wt%). The serrate characteristic of many sulfide crystal shapes in SEM images (Fig. 3) clearly point to marcasite, forming conjoined planar aggregates with a bead chain aspect in profile. Within olivine crystals affected only by incipient dissolution, FeS₂ aggregates can be observed in the center of narrow voids in relation to initial cracks or microfissures (Fig. 4b). Inside larger dissolution cavities in olivine, or where olivine was completely dissolved, FeS₂ precipitation is also organized as chains or planar aggregates and does not occur anywhere on a free olivine or glass surface (Figs. 3, 4, and 5). In places, where aggregates of several olivine grains are surrounded by glass matrix (Figs. 4a and 4b), XRM reveals that cavities in these associated grains may be multiply connected and form a complex pore network (Online Materials¹ Fig. S1).

The baseline-corrected and normalized Raman spectra of FeS₂ analyzed at selected locations of the polished thin section are displayed over the 200 to 600 cm⁻¹ spectral range in Figure 6. Following Vogt et al. (1983) and Lutz and Müller (1991), and considering the measured spectral resolution, the assignment of Raman bands to symmetry modes for pyrite (Py) and marcasite (Mrc) has been made as follows: 324 cm⁻¹ (combined A_g^{Mrc}, B_{2g}^{Mrc}, and B_{3g}^{Mrc}), 343 cm⁻¹ (E_g^{Py}), 350 cm⁻¹ (T_g^{Py}), 378 (combined A_g^{Py} and T_g^{Py}), 388 cm⁻¹ (A_g^{Mrc}), 398 cm⁻¹ (B_{1g}^{Mrc}), 430 cm⁻¹ (T_g^{Py}), 448 cm⁻¹ (B_{1g}^{Mrc}). The integrated area under the bands at about 324 and 343 cm⁻¹, respectively, was used to distinguish between pyrite and marcasite. Moreover, considering that their differential Raman scattering cross sections are similar, a quantitative approach has been performed.

The Raman spectra reveal the presence of both pyrite and marcasite in most of the analyzed locations (Fig. 6, fit results are given in Table 2). Pure pyrite spectra were observed in at least two locations (G1-11 and G1-14, Figs. 6b and 6c, respectively). A pure marcasite phase was not identified within the investigated locations of the grains. However, at G2-01 (Fig. 6d) shows that the location is comprised of about 97% marcasite along with a minor (3%) pyrite phase fraction.

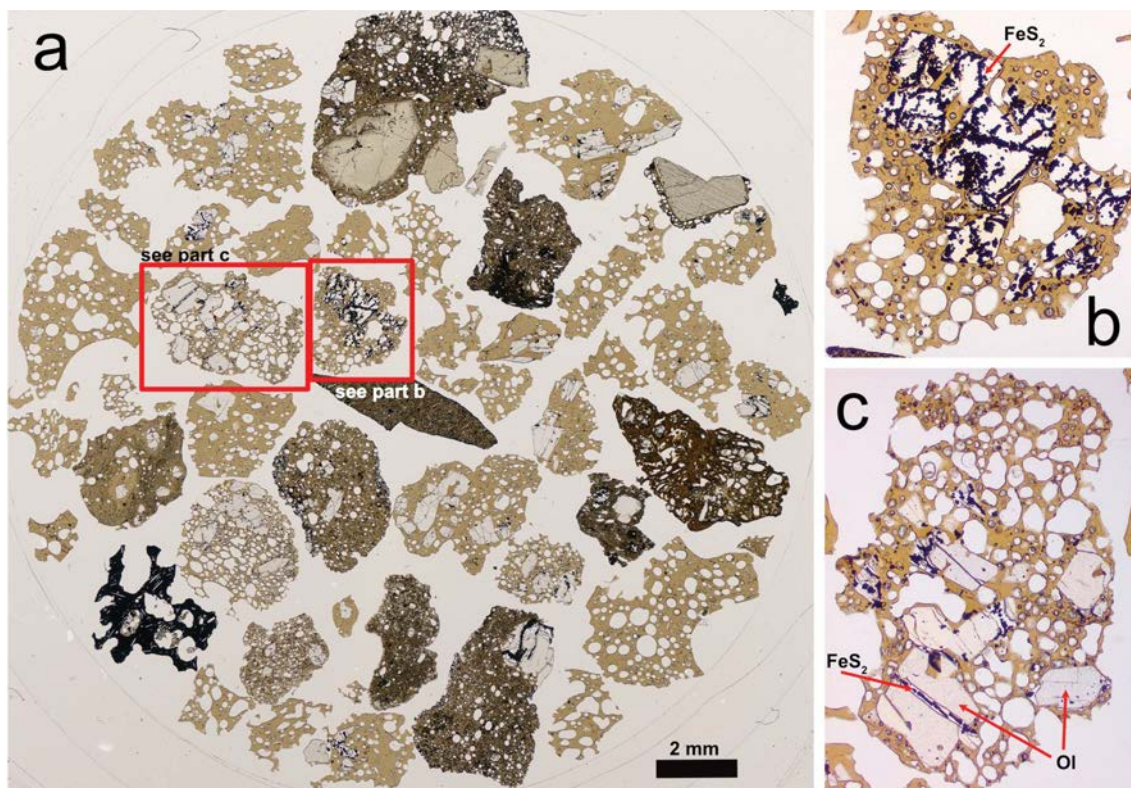


FIGURE 2. Volcanic ash particles embedded in thin section (plane-polarized light). (a) Survey of the different lithologies occurring in the volcanic ash layer. Several particles contain olivine or pyroxene crystals that exhibit sulfide-filled cavities. (b) Sulfide-filled cavity in volcanic glass where the former olivine has completely vanished. (c) Particle with olivines displaying tubular cavities, others exhibiting dissolution features at rims or end faces. (Color online.)

Relation between cavity volume and iron sulfide content

Cavities completely filled with iron sulfide were not observed in any olivine. By means of 2D (derived from BSE images, Figs. 7a–7e) and 3D (derived from reconstructed XRM image volumes, Fig. 7f) quantitative digital image analysis, iron sulfide contents in voids within olivine single crystals were found to range between 17.4 and 24.0 area%, and between 18.1 and 19.4 vol%. XRM analysis of the second sample (Online Materials¹ Fig. S1), an aggregate consisting of several attached olivine grains surrounded by a glass matrix, revealed an uneven distribution of iron sulfide precipitation. The volume fraction of iron sulfide in the largest void, extending over six olivine crystals, reached only 4.2 vol% (Fig. 7g₁). In comparison, a high-resolution scan of a region within the same aggregate reveals a degree of iron sulfide void filling of 10.1 vol% (Fig. 7g₂). Altogether, the iron sulfide precipitation in the pore space of the olivine grain aggregate is substantially less than what was observed in voids within olivine single crystals hosted in other particles (see Table 3).

Fabric relation of iron sulfide and spinel

Whereas olivine is largely affected by dissolution processes, the host glass shows only minor etch pits and spinel exhibits no indication of dissolution. Spinel occurring within the volcanic glass or in olivine material unaffected by dissolution mostly

exhibits euhedral to subhedral morphology (Fig. 8a). Likewise, spinel situated within cavities displays the very same morphology, and is mostly overgrown by the iron sulfide precipitates (Figs. 4a, 5b, and 8; Online Materials¹ Fig. S3). Moreover, detailed observations of some sites visible in Figures 4a and 8b; Online Materials¹ Fig. S3 indicate that iron sulfide growth was not initiated as alteration of spinel rims to sulfide but by overgrowths on the existing spinel surface.

Further potential nucleation sites of small sulfide particles

High-resolution 3D X-ray microscopy imaging (Fig. 8b) shows that small sulfide particles (1–2 μm) are also observed along and/or within filamentous stalks connecting cavity-centered, aligned sulfide aggregates of up to 20–60 μm diameter, analogous to the strand of a bead chain. The XRM image material (0.36 μm voxel size, compare scale information in Fig. 8b) depicts these stalks to be less X-ray attenuating than the volcanic glass and more similar to void space. As the particles investigated by 3D X-ray microscopy were neither cut nor ground and hence did not suffer any stress during sample preparation, the filamentous stalks could be preserved within the well-protected pore space inside the gravity core material in a desiccated manner. It is possible that these structures represent organic material; however, further investigations by, e.g., Raman spectrometry cannot be carried out due to the inaccessibility of the interior of this particular ash particle.

DISCUSSION

Chemical environment for olivine dissolution and iron sulfide formation

Abundant FeS_2 precipitation within cavities created by olivine dissolution indicates the availability of reactive iron (likely derived from olivine dissolution) and sulfide in solution. Indeed, evidence of hydrogen sulfide at the sample sites is twofold: (1) the perception of hydrogen sulfide smell during sample recovery and (2) the spatial association of the samples to shells of vesicomid clams on the top sediment layer. All known species of the genus *Abyssogena* have been observed in sulfide-rich habitats at hydrothermal vents and cold seeps (Krylova et al. 2010). Typically, *Abyssogena* live half-buried in the sediments, where the anterior part of the clam with the extendable foot has access to hydrogen sulfide.

Notably, the microfabric of FeS_2 precipitation within cavities resembling negative olivine crystal shapes indicates conditions of enhanced olivine dissolution. In contrast, volcanic glass adjacent to the olivine crystals was nearly unaffected by dissolution processes. Generally, basalt glass is observed to dissolve slightly more slowly (ca. 10^{-12} mol cm^{-2} s^{-1} at pH 3, and ca. 10^{-15} mol cm^{-2} s^{-1} at pH 6) (Flaathen et al. 2010; Gislason and Oelkers 2003; Oelkers and Gislason 2001) than olivine (ca. 10^{-12} mol cm^{-2} s^{-1} at pH 3, and ca. 10^{-14} mol cm^{-2} s^{-1} at pH 6) (Oelkers et al. 2018; Rimstidt et al. 2012) at 25 °C and under oxic

conditions. In contrast, the chemical environment of reducing, low-pH, sulfide-bearing fluids may enhance olivine dissolution by keeping Fe in solution and sequestering important quantities of Fe as FeS_2 . Under these conditions in situ oxidation of ferrous Fe and precipitation of ferric hydroxides at the olivine surface are impeded. These two processes may lower olivine reactivity and cause inhibition of olivine dissolution under oxic conditions (Gerrits et al. 2020). Similarly, experimental simulations by Wiggering et al. (1992) showed that subaqueous weathering under a CO_2 -rich, H_2S -bearing, hypothetical Archean atmosphere was much more intense than under today's conditions: in this acidic environment, ferrous iron released by dissolution remained in solution. The effect of the addition of H_2S to fluids on silicate dissolution has been explored by Stefánsson et al. (2011) to simulate the sequestration of H_2S into wastewater to be reinjected into the geothermal system Hellisheiði, Iceland. Their reaction path modeling showed that the accompanying decrease in pH resulted in undersaturation of Al-bearing silicates, but supersaturation with respect to sulfides.

As elements other than Fe were removed during olivine dissolution, the question arises whether the Fe in the precipitated FeS_2 was inherited entirely from the dissolved olivine material. A simple mass balance shows that complete fixation of Fe should result in ca. 20 vol% FeS_2 filling of the cavity created by olivine dissolution ($\text{Fo}_{81.5}$). Analyses of BSE images revealed iron sulfide

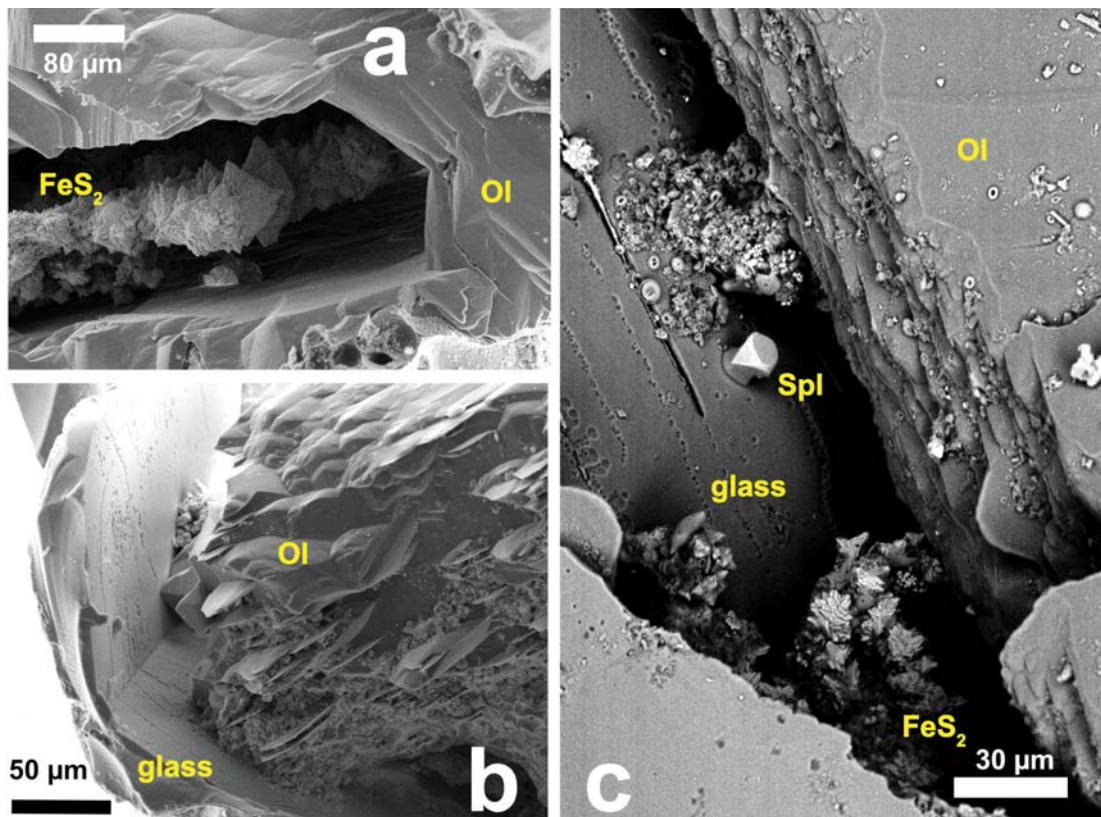


FIGURE 3. Iron sulfide mineralization in dissolution-induced cavities in olivine (SEM). (a) Cavity resembles negative olivine crystal shape, with iron sulfide mineralization as conjoined, planar aggregates. (b) In contrast to olivine (right side), volcanic glass displays only slightly corroded surfaces with small etch pits. (c) Iron sulfide growth (serrate marcasite and euhedral spinel) on volcanic glass surface. (Color online.)

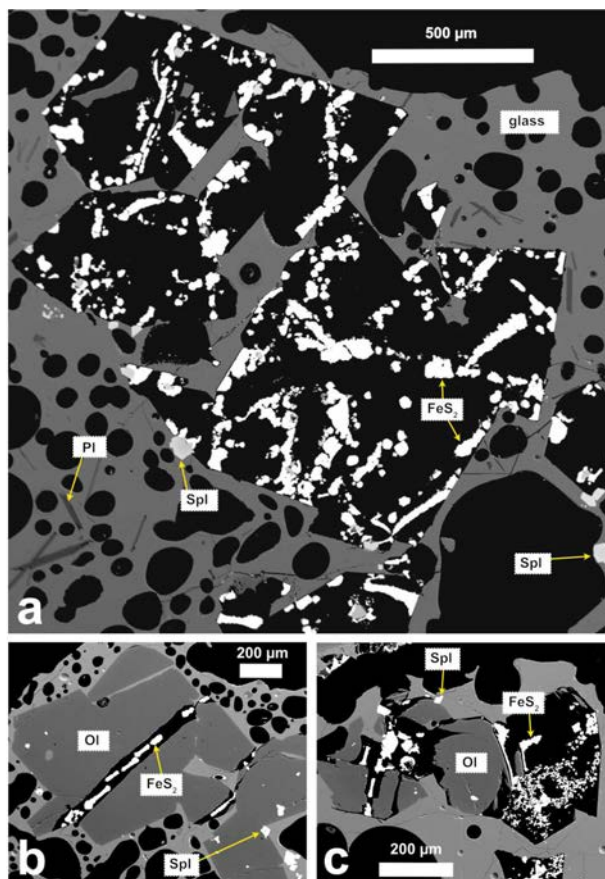


FIGURE 4. BSE images from a thin section depicts iron sulfide precipitation (white) inside cavities created by olivine dissolution. Key: Pl = plagioclase; Ol = olivine; Spl = spinel. (a) Even in cavities completely devoid of olivine, iron sulfide precipitation is organized in conjoined aggregates, forming a bead chain aspect in profile. (b) Mineralization in the center of a tubular void in an olivine crystal. (c) Iron sulfide precipitation does not occur arbitrarily and is minor or lacking on volcanic glass surfaces (neither on dissolving olivine). It does occur on some spinel surfaces, as can be seen in a. (Color online.)

fillings between 17.4 and 24.0% by area (Figs. 7a–7e; Table 3), and analyses of two cavities inside an olivine single crystal using reconstructed XRM scans yielded 18.1 and 19.4 volume percent, respectively. These results suggest that dissolution of olivine has provided all iron necessary for iron sulfide formation nearly in situ inside olivine cavities (Fig. 7f). Notwithstanding, a highly connected cavity spanning over several grouped olivine crystals exhibits far less than maximum iron sulfide fixation: Figure 7g depicts low 4.2 vol% iron sulfide precipitation within the entire pore network, increasing to 10.1 vol% within a restricted region. Apparently, not all Fe liberated from dissolved olivine was fixed by iron sulfide precipitation.

Although the serrate crystal shapes of the iron sulfides point to marcasite precipitation from solution, the coincident presence of pyrite in most places (Fig. 6) indicates a more complex FeS₂ fixation history. Locally, pyrite makes up a very high-phase fraction in the Raman spectra of the analyzed spots. While we could not find a systematic relation between marcasite/pyrite

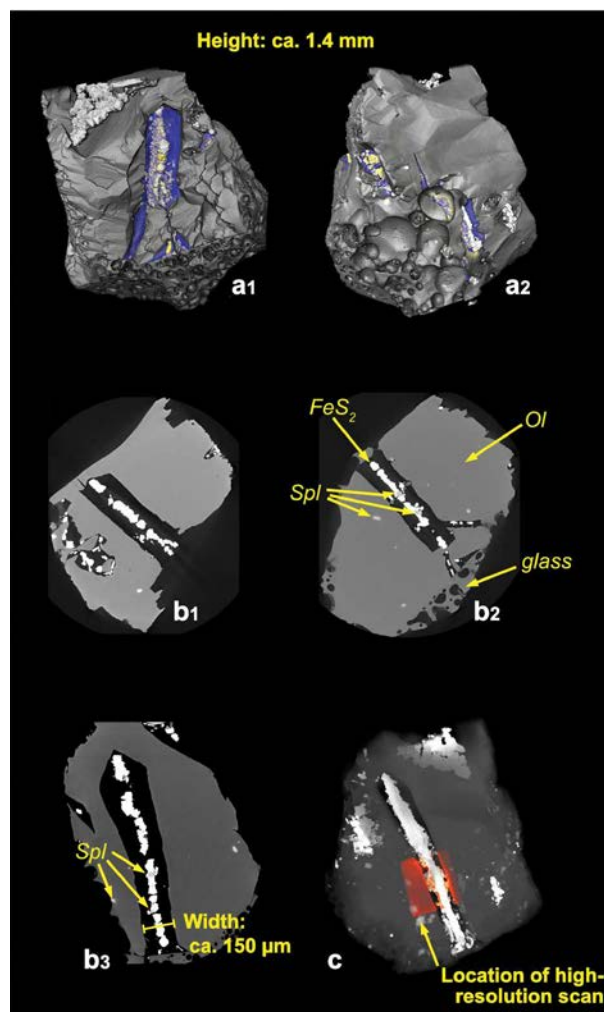


FIGURE 5. Occurrence and connectivity of voids inside a volcanic ash particle (3D X-ray microscopy, XRM). (a_{1,2}) Visualization of pore space (blue) in the volume reconstruction of an ash particle consisting of a single olivine grain and glass matrix attached. Note that this sample was analyzed with SEM in Figure 3a. (b_{1,2,3}). Reconstructed slices at different levels, displaying the bead chain aspect of iron sulfide mineralization and the location of these structures aligned in the center of the cavities. Note the occurrence of spinel in these aggregates. (c) Location of a high-resolution scan inside this particle (see Figs. 8a and 8b). Please compare also Online Materials¹ Figure S1. (Color online.)

ratios and petrographic features such as void size or crack width, our data suggest that domains with high proportions of pyrite are co-located with spinel (e.g., G-13 and G-14, Fig. 6c). In some locations concomitant red/blue-shift of the frequencies has been observed for both phases irrespective of their proportion. For instance, whereas the fitted frequencies at G1-11 correspond to those observed by Vogt et al. (1983), a general blue shift has been identified at G1-14 (see Online Materials¹ Fig. S2). The corresponding higher frequencies with broader line shapes at G1-14, in general, can be explained by slightly different unit-cell dimensions and, rather likely when considering the geochemical environment of our investigated samples, by a spread in the distribution of the degree of crystallinity and average crystallite

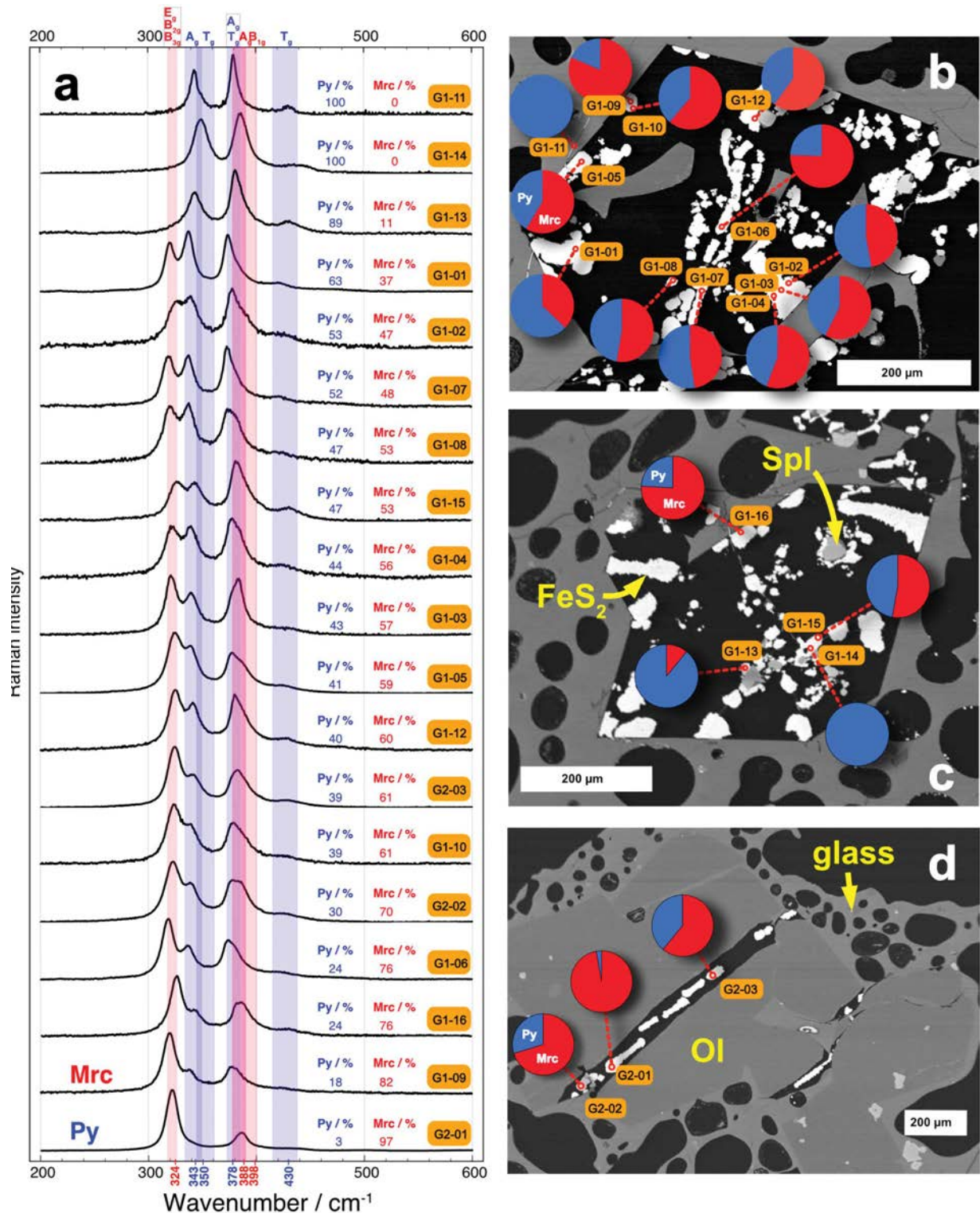


FIGURE 6. Raman spectra at selected locations on the polished thin section. (a) In most of the analyzed locations, the baseline-corrected and normalized spectra reveal the presence of both pyrite and marcasite in varying proportions. In some locations concomitant red/blue-shift of the frequencies has been observed for both phases irrespective of their proportions, which we explain in terms of slightly different average crystallite sizes. Colored letters A, B, E, and T with indices indicate Raman vibrational modes for pyrite and marcasite (colored vertical bars); see text for details. (b–d) BSE image with locations G1-01 to G1-12 (b), G1-13 to G1-16 (c), and G2-01 to G2-03, respectively. Phase proportions are indicated by pie charts. (Color online.)

TABLE 2. Raman fit frequencies ($\pm 0.1 \text{ cm}^{-1}$) and their assignments for the respective symmetry species obtained from the deconvoluted spectra of FeS_2 at selected locations of the polished thin sections as labeled in Figure 6

Location (Grain, Spot)	$A_g(\text{Mrc})/B_{2g}(\text{Mrc})/B_{3g}(\text{Mrc})$	$E_g(\text{Py})$	$T_g(\text{Py})$	$A_g(\text{Py})/T_g(\text{Py})$	$A_g(\text{Mrc})$	$B_{1g}(\text{Mrc})$	$T_g(\text{Py})$	$B_{1g}(\text{Mrc})$	Py /%	Mrc /%
G1-01	319.51	336.92	355.19	373.36	379.81	–	418.75	–	63	37
G1-02	324.05	339.05	352.68	378.81	–	393.82	423.80	463.12	53	47
G1-03	320.98	339.82	344.98	382.92	381.15	–	426.52	–	43	57
G1-04	321.15	338.95	352.23	378.48	–	398.00	423.64	–	44	56
G1-05	324.03	339.74	361.46	376.24	385.58	398.27	420.91	–	41	59
G1-06	318.41	337.64	354.92	373.28	379.69	396.61	419.77	452.43	24	76
G1-07	317.54	336.28	354.07	372.18	380.42	–	415.68	446.30	52	48
G1-08	319.26	336.80	353.09	373.73	378.56	398.00	417.68	–	47	53
G1-09	319.17	338.57	354.15	378.15	390.75	398.00	421.89	–	18	82
G1-10	323.22	339.35	352.02	378.88	–	390.35	425.46	–	39	61
G1-11	–	342.21	350.20	378.61	389.56	–	429.31	–	100	0
G1-12	324.56	341.71	360.00	380.05	386.85	–	426.23	–	40	60
G1-13	324.00	342.19	350.00	380.00	388.00	401.24	430.22	–	89	11
G1-14	–	348.76	–	385.32	–	395.22	438.85	–	100	0
G1-15	326.10	343.96	361.46	380.52	385.98	399.92	427.56	–	47	53
G1-16	324.86	343.10	361.76	380.43	387.54	401.75	426.00	–	24	76
G2-01	324.56	341.71	360.00	378.00	380.05	386.85	426.23	–	3	97
G2-02	322.39	339.97	357.12	376.26	385.94	398.00	423.87	–	30	70
G2-03	324.19	342.16	356.95	379.62	383.65	398.00	427.81	–	39	61

Note: The symmetry species of the pyrite (Py) and marcasite (Mrc) are given.

size. Of note, Bryant et al. (2018) suggested that the red shift of band positions can be associated with laser-induced heating during Raman investigations, and that variations in the ratios of band intensities can arise due to differing crystallographic orientations of the Raman-active species with respect to the laser's dominant polarization plane.

Can the observation of coexisting pyrite and marcasite be related to phase transformations induced by Raman laser heating? Xi et al. (2019) discussed such thermal transformations and found that the minimum laser power for these reactions to occur is 2.87 mW (see their Fig. 6 and related text). In contrast, our Raman investigations were carried out with a substantially reduced laser power on the sample surface of about 0.33 mW (by the usage of a neutral density filter, see methods section). Moreover, during the measurements, we could not observe any change of either intensity of a given band or the appearance/disappearance of any band. For these reasons we exclude transformation induced by laser heating during our Raman analyses. However, variable proportions of Mrc and Py in the sulfide aggregates of the present study could be related to the marcasite to pyrite transformation under hydrothermal conditions. In a recent study of an interface-coupled dissolution-reprecipitation reaction involving pyrrhotite, Yao et al. (2021) observed that the Mrc to Py transformation in small particles (<100 nm) can occur within a few months at 210 °C, a pH of 1, and a high-sulfide saturation index. Although we do not know how these conditions relate to those of our study, the experiments of Yao et al. (2021) suggest that post-crystallization transformation of marcasite to pyrite may have contributed to the variable Mrc and Py proportions observed.

Commonly, marcasite is associated with iron sulfide formation at lower pH than estimated for pyrite formation (recently summarized in Yao et al. 2020, 2021). Precipitation of marcasite from hydrothermal solutions has been observed in experimental studies at pH values of 5 or lower (Murowchick and Barnes 1986; Schoonen and Barnes 1991). However, in more complex experimental environments or natural systems, inhomogeneities can catalyze heterogeneous nucleation: Qian et al. (2011) suggested that a coupled dissolution-reprecipitation reaction can have marcasite replace pyrrhotite at the low-sulfide activity of the fluid and does

not require low pH. These authors also found that marcasite formed only on pyrrhotite grains, not on other parts of their experimental autoclaves, which suggests epitaxial nucleation at an incipient reaction stage. Significant in respect to the iron sulfide microfabric relations observed in this study, experiments of Schoonen and Barnes (1991) indicate that in acidic solutions below 100 °C nucleation of FeS_2 is actually inhibited, although the growth of existing marcasite and pyrite is possible under these conditions.

The microfabric of conjoined, variably intergrown crystals (Barbee et al. 2020; Welsch et al. 2013) constituting the iron sulfide aggregates of our study suggests an increased reaction affinity (ΔG_r), at least during early growth of the center layer (Figs. 3, 7, and 8). This is in conspicuous contrast to the absence of nucleation sites of FeS_2 on volcanic glass. Thus, the presence and intergrowth of two different iron sulfides do not necessarily reflect changes in boundary conditions such as temperature or pH. It is also unlikely to reflect the transformation of one phase into the other, as we have discussed above. It could, however, indicate a formation pathway that successfully overcame hindered nucleation. Pyrite may have grown first, and subsequent fixation of FeS_2 may have occurred as marcasite precipitation, producing the serrate shapes observed. Potential indications of this growth sequence are: (1) the higher pyrite fraction in mixed iron sulfide analyses near spinel (which is located prevalently in the center of the precipitates), and (2) the serrate, marcasite-like shape of the outer parts of the iron sulfide precipitates (presumably fixated later than the interior parts).

Control on the sites of iron sulfide precipitation

Our observation that FeS_2 precipitation is completely lacking at the surfaces of volcanic glass and dissolving olivine evidently corroborates the finding of Schoonen and Barnes (1991) that the rate of homogeneous FeS_2 nucleation is negligible in acidic solutions. Instead, we observe that iron sulfide precipitation at an incipient stage is inevitably linked to the presence of spinel inclusions in olivine (Figs. 4a and 8; Online Materials¹ Fig. S3). In particular, Figure 8b₂ depicts a stage of incipient growth of iron sulfide on spinel. Regarding the inventory of available sites for heterogeneous FeS_2 nucleation, spinel surfaces apparently provide the preferred

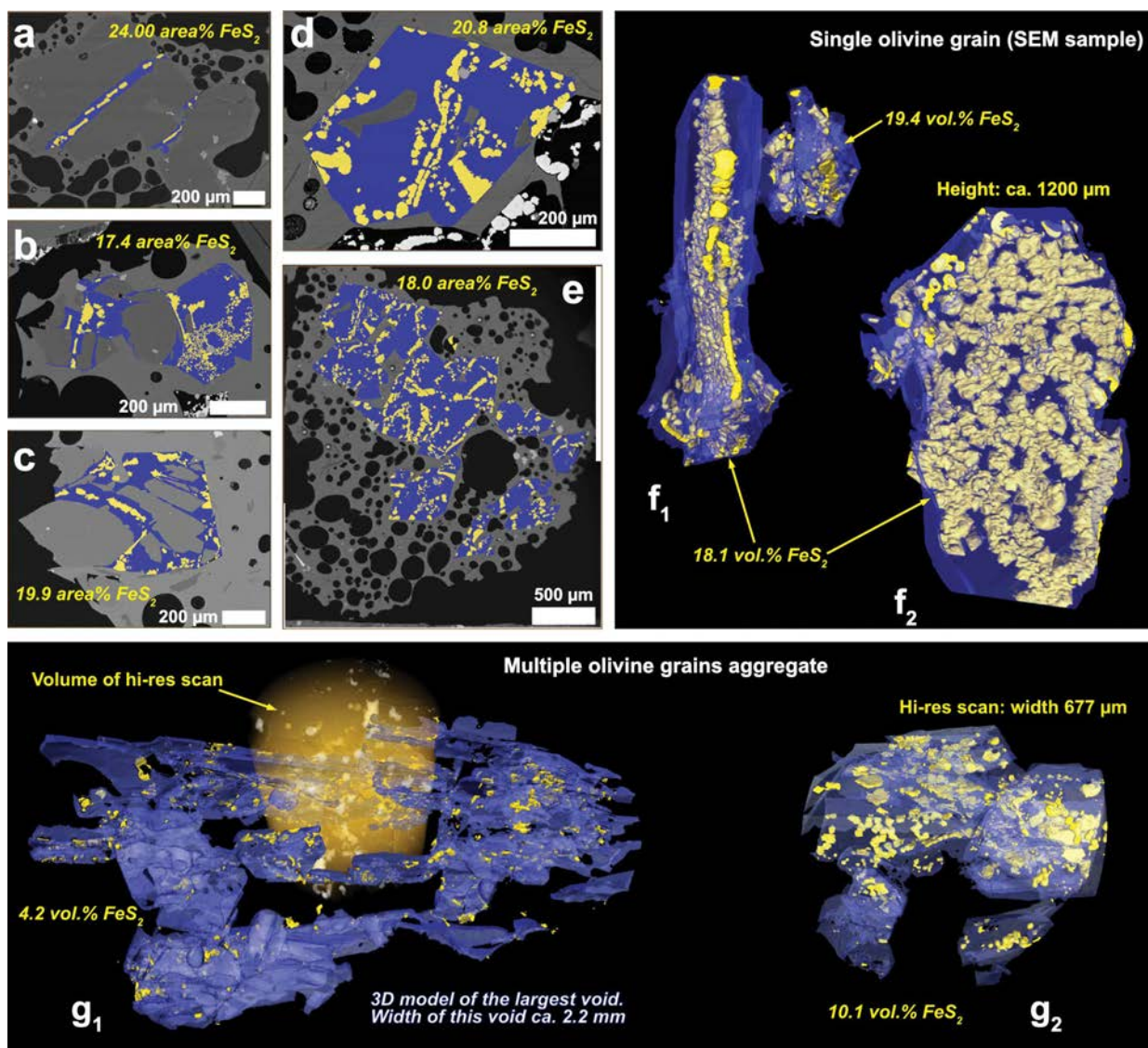


FIGURE 7. 2D and 3D quantitative image analysis of iron sulfide precipitation (yellow) inside cavities (blue) created by olivine dissolution. (a–e) 2D analyses of selected cavities using BSE images. (f_{1,2}) and (g_{1,2}) 3D analyses of selected cavities using reconstructed XRM scans. (Color online.)

locality for heterogeneous nucleation since olivine is dissolving, and volcanic glass is obviously not favorable to iron sulfide precipitation. The latter observation is particularly important as it demonstrates the requirement of a pre-existing crystal structure for heterogeneous nucleation of iron sulfide to occur.

The idea of heterogeneous nucleation of marcasite is corroborated by the experimental results of Qian et al. (2011), who reported epitaxial marcasite nucleation exclusively on pyrrhotite grains and not on other parts of their autoclaves. Furthermore, we show that FeS₂ precipitation occurred dominantly where a spinel surface is connected to a cavity within dissolved olivine. After heterogeneous nucleation on spinel grains has occurred, iron sulfide can grow under conditions at which rates of homogeneous nucleation are still low. If spinel surfaces are critical to the nucleation of iron sulfide, then a relationship between the abundance of both phases may be expected. Indeed, we found that regions with minor spinel

exposed at olivine dissolution surfaces within the interconnected pore space of the olivine aggregates show less FeS₂ precipitation (see Online Materials¹ Fig. S1).

These interpretations are in accordance with the results of 3D X-ray microscopy (Figs. 8; Online Materials¹ Fig. S3), which unveiled nucleation sites on spinel, development of cavities around spinel grains near the olivine dissolution surface, and the organization of FeS₂ aggregates with spinel crystals enclosed therein. Raman spectroscopy showed that FeS₂ occurrences close to spinel grains are dominated by pyrite. This supports our earlier notion that iron sulfide formation initially proceeds via heterogeneous growth of pyrite on spinel (both of cubic symmetry), joined by marcasite precipitation in later stages. Heterogeneous FeS₂ nucleation may occur directly on the spinel surface. It is conceivable that an alternative iron sulfide formation pathway occurs via thin layers of greigite (Fe₃S₄; the thio-spinel of iron), a phase not

TABLE 3. Percentage of iron sulfide content in relation to the hosting cavity

Cavity description	Sulfide area% /vol%	Source	Part of Figure 7
Ol in thin section	24.0	BSE	a
Ol in thin section	17.4	BSE	b
Ol in thin section	19.9	BSE	c
Ol in thin section	20.8	BSE	d
Ol in thin section	18.0	BSE	e
Largest void in single Ol grain	18.1	XRM	f ₁
2nd largest void in single Ol grain	19.4	XRM	f ₂
Largest connected void, spanning over multiple olivines	4.2	XRM	g ₁
Close-up of the above	10.1	XRM	g ₂

Notes: Ol = olivine; BSE = backscattered image (2D quantitative image analysis); XRM = 3D X-ray microscopy (3D quantitative image analysis).

uncommon to submarine iron sulfide formation in a sedimentary setting (Rickard 2012; Roberts 2015). In this case, greigite rather than FeS₂ may have been the phase to grow initially on the spinel surface, providing an opportunity for subsequent nucleation of pyrite. However, we did not detect any greigite by our EPMA

or Raman investigations at the resolution used. At this point, we cannot resolve by which mechanisms heterogeneous nucleation actually occurred and whether epitaxial growth played a major role.

Thermodynamic/kinetic constraints concerning formation pathway and timing

We conducted reaction path model calculations to determine if the formation of pyrite or marcasite is plausible in a system in which seawater interacts with basaltic glass, olivine, and organic carbon. The results in Figure 9 shows that pyrite is indeed expected to be the dominant secondary mineral in the early stages of evolution. Celadonite and smectite clay are predicted to form later in the sequence as the pool of solutes is more strongly affected by elements released by (slow) glass dissolution. When organic carbon is oxidized, and the reducing power for sulfate reduction is exhausted in the model, pyrite formation slows and eventually gives way to the formation of goethite and clay. In the mature stages of alteration, clay, oxide, and carbonate dominate

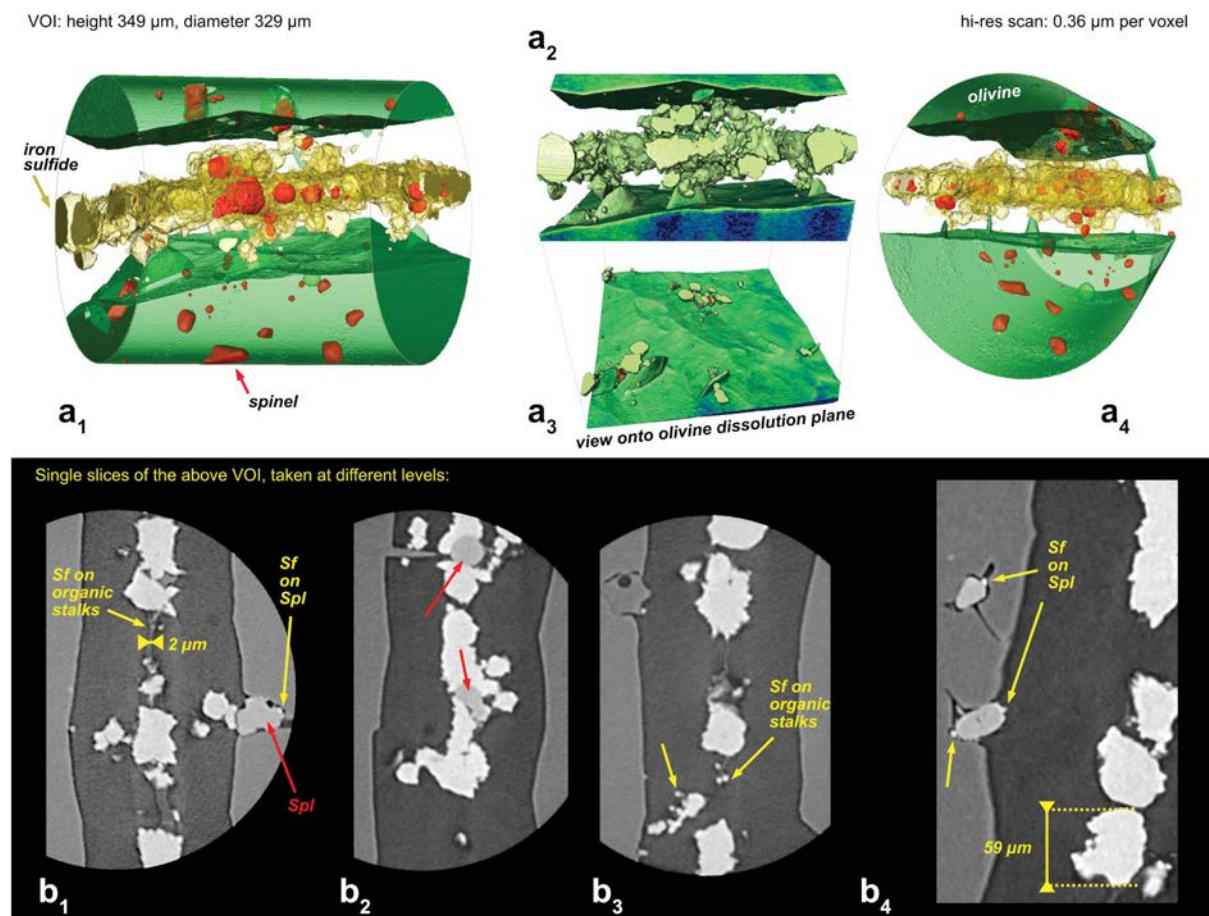


FIGURE 8. Results from high-resolution XRM scans showing microfabric of olivine dissolution and FeS₂ precipitation processes, with particular consideration of spinel occurrence. Key: Spl = spinel; Sf = sulfide. (a) Semitransparent rendering of olivine (green) and iron sulfide reveals presence of spinel inside the FeS₂ precipitates (a₁, a₄). (a₂) Opaque rendering of this layer highlights the serrate characteristic of iron sulfide in this particular piece (see also Fig. 3a). (a₃) 3D view of an olivine dissolution surface, encompassing the iron sulfide mineralization. Note the tiny bridges that in places connect the sulfide layer with the retreated olivine dissolution surface. (b) Reconstructed image slices of the volume of interest in (a) unveil sulfide growth features, such as nucleation sites both on spinel and filamentous structures, development of cavities around spinel grains near the olivine dissolution surface, the organization of iron sulfide aggregates, and spinel crystals enclosed therein. For localization of the high-resolution scan please refer to Figure 5. Please compare also Online Materials¹ Figure S3. (Color online.)

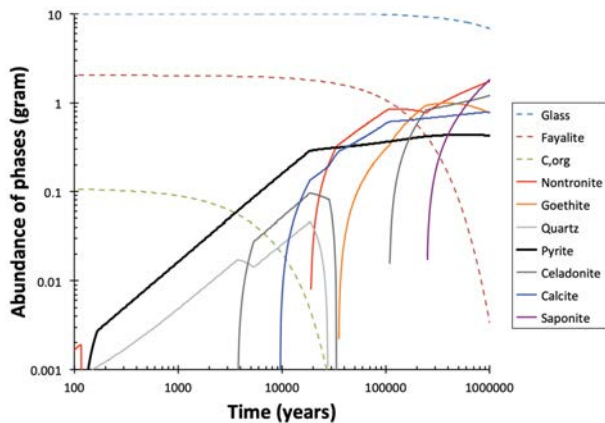


FIGURE 9. Results of a reaction path model calculation showing the possible timing of pyrite (or marcasite) formation. See text for model details. (Color online.)

the predicted assemblage of secondary minerals. This is consistent with what is observed in altered basalts from the ocean crust (e.g., Alt 1995). Of particular importance in the modeling results is the episode between 100 and 10,000 years, during which pyrite is predicted to dominate the secondary mineral assemblage (Fig. 9). The assumption of reaction rates decreasing in the order of organic carbon, olivine, and glass is critical for the model to predict abundant pyrite formation in the first couple of thousands of years. The model predicts organic carbon will be

oxidized by sulfate, which is turned to sulfide. Iron is released from olivine dissolution, which is faster than the dissolution of glass by roughly an order of magnitude (Oelkers et al. 2018; Oelkers and Gislason 2001). Iron then reacts with sulfide from bacterial sulfate reduction to form pyrite (or marcasite). Distinguishing between the two FeS_2 polymorphs in the model does not make any difference. Marcasite is predicted to form when pyrite formation is suppressed in the model, and its abundance curve is indistinguishable from that of pyrite in Figure 9.

The absolute reaction rates are poorly constrained, but our assumed factors of 10 and 500 by which the dissolution of olivine and reaction of organic carbon, respectively, are faster than glass dissolution are reasonable. Organic carbon reaction kinetics in the diagenetic system is controlled by microbial metabolism, as the reduced carbon is the electron donor in the catabolic reaction that uses sulfate as terminal electron acceptor. By as of yet unidentified mechanisms, the metabolic products of microbial sulfate reduction may enhance the difference in dissolution rates between olivine and volcanic glass. The more accelerated olivine dissolution is relative to the rate of basalt glass dissolution, the more pronounced the dominance of pyrite in the secondary mineral assemblage in the incipient alteration stage before clay-oxide-carbonate alteration eventually takes over. The mechanisms behind this enhanced weathering of olivine in the sulfate-reduction zone need to be examined and may involve microbially produced chelators that help solubilize the iron.

The predicted period for dominant pyrite formation between 100 and 10,000 years is consistent with a presumably young

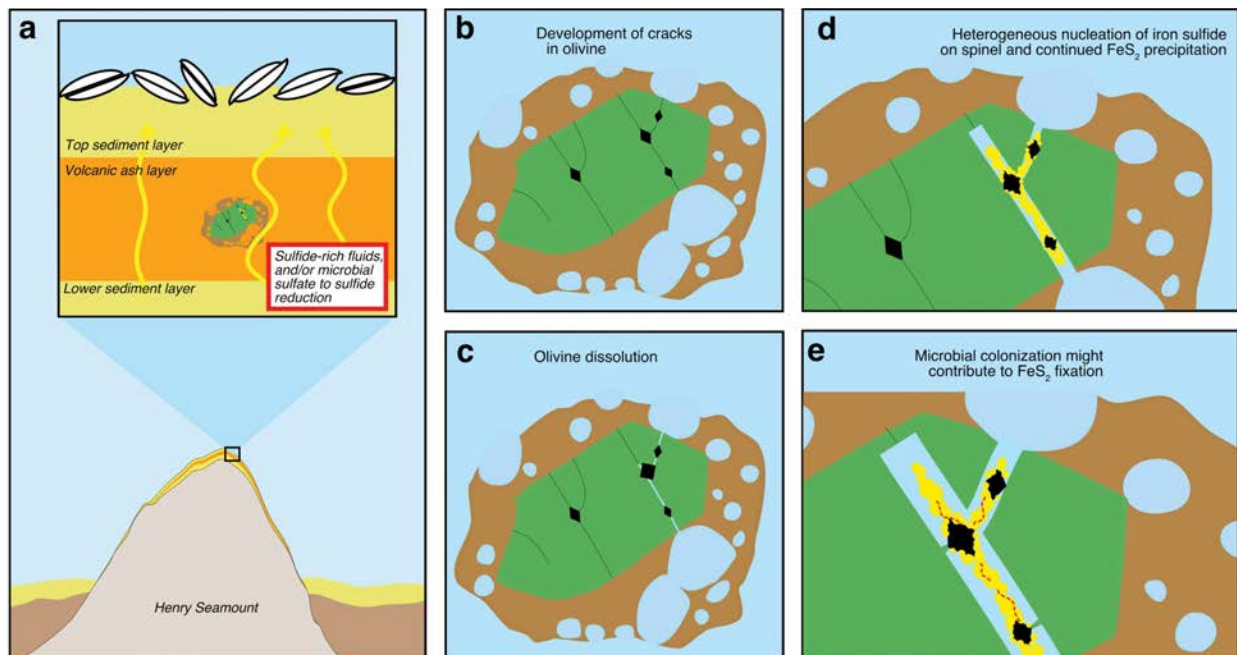


FIGURE 10. Conceptual model for rapid olivine dissolution and iron sulfide formation. (a) Cartoon representation of the chemical environment for rapid olivine dissolution and iron sulfide formation. Widespread occurrence of shells of vesicomyid clams (genus *Abyssogena*) at the sampling site indicate the presence of sulfide-rich fluids. (b–e) Iron sulfide formation involves: (b) development of cracks in olivine, preferentially around spinel, (c) infiltration of reducing sulfide-bearing solutions and initiation of olivine dissolution, (d) heterogeneous nucleation of FeS_2 preferably as pyrite on spinel and continued growth of FeS_2 aggregates. (e) Eventually, colonization of sulfate-reducing bacteria may add an additional path for microbial iron fixation. (Color online.)

age of the fresh volcanic ash samples studied here. Precise age dates are lacking, but the spatial association between ash and clamshell fields led Klügel et al. (2020) to hypothesize that hydrothermal circulation and consequent colonization by vesicomid *Abyssogeta* clams were initiated by one or more pulses of volcanic activity. The age of the ash may thus be close to the radiocarbon ages of clamshells, which are in the range of a few ka to <20 ka (Klügel et al. 2011, 2020). This age range would be consistent with a sediment coverage of the ash by <13 cm in the gravity core (Fig. 1b), and <20 cm in nearby grab samples, if a sedimentation rate of <7 cm/ka (Gee et al. 2001) is assumed.

Conceptual model for iron sulfide formation

A most striking feature of the observed dissolution-precipitation reaction is that the iron sulfide fillings are organized in a bead chain aspect and are centered in the cavities (Figs. 7 and 8). Here we present a conceptual model for iron sulfide formation from rapidly dissolving olivine (Fig. 10).

The key features are intracrystalline cracks within the olivine crystals, along which low-pH, H₂S-bearing fluids could percolate (Fig. 10b). These cracks appear to develop preferentially around spinel (see Welsch et al. 2013, Fig. 11 therein), likely during the submarine eruption event or during magma ascent and decompression as a result of different elastic properties and thermal expansion of spinel and host olivine. Facilitated by the high solubility of Fe²⁺ in the reduced fluids, rapid olivine dissolution proceeds at grain boundaries and at surfaces exposed by the cracks. By heterogeneous nucleation of FeS₂ on spinel grains, pyrite and possibly marcasite precipitation can begin within very thin fissures at an early stage of dissolution once Fe²⁺ is available (Figs. 10c–10d). Continued olivine dissolution enlarges these cracks forming cavities, and continued nucleation and growth of pyrite and/or marcasite form aggregates centered within the growing gaps. A cartoon representation of the chemical environment for rapid olivine dissolution and iron sulfide formation is presented in Figure 10a.

Possible role of microbial interactions for olivine dissolution and/or FeS₂ precipitation

Although there are many studies that report microbial or fungal mediation of mineral dissolution reactions (Gerrits et al. 2020; Thiel et al. 2019; Welch and Banfield 2002), the process of rapid olivine dissolution was not necessarily directly mediated by sub-seafloor life. The observation of smooth dissolution surfaces with negative crystal shapes points to a crystallographic-mineralogical control rather than microbe-aided olivine dissolution. Whereas microbial reduction of sulfate to sulfide may have produced the reducing environment required for the dissolution, an abiotic sulfide source from depth is also possible (Klügel et al. 2020).

The precipitation of iron sulfide aggregates investigated in this study may well be understood by epitaxial nucleation related to spinel and continued iron sulfide precipitation from low-pH and H₂S-bearing fluids (Fig. 10). When microbes exert crystallochemical control over the nucleation and growth of the mineral particles, distinctly different particle morphologies and narrow size distributions can develop (Bazylinski and Frankel 2003). For instance, magnetotactic bacteria intracellularly produce greigite particles in the size range of 100 nm (Heywood et al. 1991; Posfai

et al. 1998) that are aligned in micrometer-sized multiple chains, and extracellular biomineralization of greigite was reported by Gorlas et al. (2018). Furthermore, biomineralization producing extracellular, filamentous structures (Chan et al. 2011; Emerson et al. 2007; Hallbeck and Pedersen 1991; Vigliaturo et al. 2020) has been linked to Fe(III)-rich filaments observed in the geological record (Alt 1988; Hofmann et al. 2008; Little et al. 2004; Slack et al. 2007). Therefore, in the rock studied here, late colonization of sulfate-reducing bacteria may eventually have added a further path of iron fixation (Figs. 8b and 10e): fibrous structures with small sulfide particles in extracellular stalks could well contribute as nuclei for later iron sulfide growth sites.

IMPLICATIONS

Under sulfidic conditions, dissolution of olivine at the seafloor can be rapid and greatly exceed glass dissolution rates. These conditions can be due to microbial respiration of seawater sulfate to sulfide in marine sediments or to an influx of hydrothermally sourced (abiotic) sulfide. The sulfide-bearing fluids enhance olivine dissolution by preventing the formation of hydrous ferric oxide layers and sequestering iron as FeS₂.

An important prerequisite of the effective fixation of Fe as iron sulfide may be the opportunity for heterogeneous nucleation. There is no evidence for homogenous nucleation of FeS₂. Instead, initial pyrite precipitation was facilitated by heterogeneous nucleation on spinel grains exposed to the void space. Subsequent removal of Fe from solution occurred exclusively by pyrite and marcasite precipitation as an overgrowth on existing iron sulfide aggregates.

The delicate structures of FeS₂ within voids created by olivine dissolution have not been described before. They may represent a transient feature in seafloor alteration, as progressive dissolution of volcanic glass causes the formation of Fe-oxyhydroxides and clay minerals (iddingsitization), which is the commonly observed alteration feature in seafloor basalts. The filling of former olivine voids by these later alteration phases and/or carbonates may obscure the earlier formed iron sulfides, making them a comparatively rare observation.

ACKNOWLEDGMENTS AND FUNDERS

We gratefully acknowledge the reviews of Benjamin Malvoisin and an unknown reviewer. W.A.K. and W.B. are grateful for funding by DFG Reinhart Koselleck Project (grant no. BA 1605/10-1), and A.K. acknowledges the funding of the Henry Seamount research by DFG (grant no. KL1313/18-1).

REFERENCES CITED

- Alt, J.C. (1988) Hydrothermal oxide and nontronite deposits on seamounts in the eastern Pacific. *Marine Geology*, 81, 227–239.
- (1995) Subseafloor processes in mid-ocean ridge hydrothermal systems. *Seafloor Hydrothermal Systems: Physical, Chemical, Biological, and Geological Interactions*, 85–114.
- Barbee, O., Chesner, C., and Deering, C. (2020) Quartz crystals in Toba rhyolites show textures symptomatic of rapid crystallization. *American Mineralogist*, 105, 194–226.
- Bazylinski, D.A., and Frankel, R.B. (2003) Biologically controlled mineralization in prokaryotes. *Biomineralization*, 54, 217–247.
- Bethke, C.M. (1996) *Geochemical Reaction Modeling*. Oxford University Press.
- Bryant, R.N., Pasteris, J.D., and Fike, D.A. (2018) Variability in the Raman spectrum of unpolished growth and fracture surfaces of pyrite due to laser heating and crystal orientation. *Applied Spectroscopy*, 72, 37–47.
- Chan, C.S., Fakra, S.C., Emerson, D., Fleming, E.J., and Edwards, K.J. (2011) Lithotrophic iron-oxidizing bacteria produce organic stalks to control mineral growth: Implications for biosignature formation. *The ISME Journal*, 5, 717–727.
- Emerson, D., Rentz, J.A., Lilburn, T.G., Davis, R.E., Aldrich, H., Chan, C., and Moyer, C.L. (2007) A novel lineage of proteobacteria involved in formation of marine Fe-oxidizing microbial mat communities. *PLOS One*, 2, e667.

- Flaathen, T.K., Gislason, S.R., and Oelkers, E.H. (2010) The effect of aqueous sulphate on basaltic glass dissolution rates. *Chemical Geology*, 277, 345–354.
- Gee, M.J.R., Watts, A.B., Masson, D.G., and Mitchell, N.C. (2001) Landslides and the evolution of El Hierro in the Canary Islands. *Marine Geology*, 177, 271–293.
- Gerrits, R., Pokharel, R., Breitenbach, R., Radnik, J., Feldmann, L., Schuessler, J.A., von Blanckenburg, F., Gorbushina, A.A., and Schott, J. (2020) How the rock-inhabiting fungus *K. petricola* A95 enhances olivine dissolution through attachment. *Geochimica et Cosmochimica Acta*, 282, 76–97.
- Gislason, S.R., and Oelkers, E.H. (2003) Mechanism, rates, and consequences of basaltic glass dissolution: II. An experimental study of the dissolution rates of basaltic glass as a function of pH and temperature. *Geochimica et Cosmochimica Acta*, 67, 3817–3832.
- Gorlas, A., Jacquemot, P., Guigner, J.-M., Gill, S., Forterre, P., and Guyot, F. (2018) Greigite nanocrystals produced by hyperthermophilic archaea of *Thermococcales* order. *PLOS One*, 13, e0201549.
- Hallbeck, L., and Pedersen, K. (1991) Autotrophic and mixotrophic growth of *Gallionella ferruginea*. *Journal of General Microbiology*, 137, 2657–2661.
- Helgeson, H.C., Delany, J.M., Nesbitt, H.W., and Bird, D.K. (1978) Summary and critique of the thermodynamic properties of rock-forming minerals. *American Journal of Science*, 278-A.
- Heywood, B.R., Mann, S., and Frankel, R.B. (1991) Structure, morphology and growth of biogenic greigite (Fe₃S₄). *Materials Research Society Proceedings*, 218, 93–108.
- Hofmann, B.A., Farmer, J.D., von Blanckenburg, F., and Fallick, A.E. (2008) Subsurface filamentous fabrics: an evaluation of origins based on morphological and geochemical criteria, with implications for exopaleontology. *Astrobiology*, 8, 87–117.
- Hunger, S., and Benning, L.G. (2007) Greigite: A true intermediate on the polysulfide pathway to pyrite. *Geochemical Transactions*, 8, 1.
- Jarosewich, E., Nelen, J., and Norberg, J. (1980) Reference samples for electron microprobe analysis. *Geostandards and Geoanalytical Research*, 4, 43–47.
- Jiang, W.-T., Homg, C.-S., Roberts, A.P., and Peacor, D.R. (2001) Contradictory magnetic polarities in sediments and variable timing of neof ormation of authigenic greigite. *Earth and Planetary Science Letters*, 193, 1–12.
- Johnson, J.W., Oelkers, E.H., and Helgeson, H.C. (1992) SUPCRT92: A software package for calculating the standard molal thermodynamic properties of minerals, gases, aqueous species, and reactions from 1 to 5000 bar and 0 to 1000 °C. *Computers & Geosciences*, 18, 899–947.
- Klügel, A., Hansteen, T.H., van den Bogaard, P., Strauss, H., and Hauff, F. (2011) Holocene fluid venting at an extinct Cretaceous seamount, Canary archipelago. *Geology*, 39, 855–858.
- Klügel, A., Villinger, H., Römer, M., Kaul, N., Krastel, S., Lenz, K.-F., and Wintersteller, P. (2020) Hydrothermal activity at a cretaceous seamount, canary archipelago, caused by rejuvenated volcanism. *Frontiers in Marine Science*, 7.
- Klügel, A., Bachmann, K., Barrett, R., Büttner, H., Fleischmann, T., Fraile Nuez, E., Held, P., Jähmlich, H., Kaul, N., Kramer, L., and others. (2018) METEOR Fahrtbericht/Cruise Report M146, Henry Seamount Seepage Exploration (HESSE), Recife (Brazil), Las Palmas de Gran Canaria (Spain), March 17–April 16, 2018. Gutachterpanel Forschungsschiffe.
- Krylova, E.M., Sahling, H., and Janssen, R. (2010) Abyssogena: a new genus of the family Vesicomidae (bivalvia) *Journal of Molluscan Studies*, 76, 107–132.
- Little, C.T.S., Glynn, S.E.J., and Mills, R.A. (2004) Four-hundred-and-ninety-million-year record of bacteriogenic iron oxide precipitation at seafloor hydrothermal vents. *Geomicrobiology Journal*, 21, 415–429.
- Lutz, H.D., and Müller, B. (1991) Lattice vibration spectra. LXVIII. Single-crystal Raman spectra of marcasite-type iron chalcogenides and pnictides, FeX₂ (X=S, Se, Te; P, As, Sb). *Physics and Chemistry of Minerals*, 18, 265–268.
- Middelburg, J.J. (1989) A simple rate model for organic matter decomposition in marine sediments. *Geochimica et Cosmochimica Acta*, 53, 1577–1581.
- Murowchick, J.B., and Barnes, H.L. (1986) Marcasite precipitation from hydrothermal solutions. *Geochimica et Cosmochimica Acta*, 50, 2615–2629.
- Oelkers, E.H., and Gislason, S.R. (2001) The mechanism, rates and consequences of basaltic glass dissolution: I. An experimental study of the dissolution rates of basaltic glass as a function of aqueous Al, Si and oxalic acid concentration at 25 °C and pH=3 and 11. *Geochimica et Cosmochimica Acta*, 65, 3671–3681.
- Oelkers, E.H., Declercq, J., Saldi, G.D., Gislason, S.R., and Schott, J. (2018) Olivine dissolution rates: A critical review. *Chemical Geology*, 500, 1–19.
- Passier, H.F., Middelburg, J.J., de Lange, G.J., and Böttcher, M.E. (1997) Pyrite contents, microtextures, and sulfur isotopes in relation to formation of the youngest eastern Mediterranean sapropel. *Geology*, 25, 519–522.
- Posfai, M., Buseck, P.R., Bazylinski, D.A., and Frankel, R.B. (1998) Iron sulfides from magnetotactic bacteria; structure, composition, and phase transitions. *American Mineralogist*, 83, 1469–1481.
- Qian, G., Xia, F., Brugger, J., Skinner, W.M., Bei, J., Chen, G., and Pring, A. (2011) Replacement of pyrrhotite by pyrite and marcasite under hydrothermal conditions up to 220 °C: An experimental study of reaction textures and mechanisms. *American Mineralogist*, 96, 1878–1893.
- Rickard, D. (2012) Chapter 5—Metastable sedimentary iron sulfides. In D. Rickard, Ed., *Developments in Sedimentology*, 65, p. 195–231. Elsevier.
- Rimstidt, J.D., Brantley, S.L., and Olsen, A.A. (2012) Systematic review of forsterite dissolution rate data. *Geochimica et Cosmochimica Acta*, 99, 159–178.
- Roberts, A.P. (2015) Magnetic mineral diagenesis. *Earth-Science Reviews*, 151, 1–47.
- Roberts, A.P., Jiang, W.-T., Florindo, F., Homg, C.-S., and Laj, C. (2005) Assessing the timing of greigite formation and the reliability of the Upper Olduvai polarity transition record from the Crostolo River, Italy. *Geophysical Research Letters*, 32.
- Ryan, W.B.F., Carbotte, S.M., Coplan, J., O'Hara, S., Melkonian, A., Arko, R., Weissel, R.A., Ferrini, V., Goodwillie, A., Nitsche, F., and others. (2009) Global Resolution Topography (GMRT) synthesis data set. *Geochemistry, Geophysics, Geosystems*, 10, Q03014.
- Schoonen, M.A.A., and Barnes, H.L. (1991) Reactions forming pyrite and marcasite from solution: I. Nucleation of FeS₂ below 100 °C. *Geochimica et Cosmochimica Acta*, 55, 1495–1504.
- Slack, J.F., Grenne, T., Bekker, A., Rouxel, O.J., and Lindberg, P.A. (2007) Suboxic deep seawater in the late Paleoproterozoic: Evidence from hematitic chert and iron formation related to seafloor-hydrothermal sulfide deposits, central Arizona, U.S.A. *Earth and Planetary Science Letters*, 255, 243–256.
- Stefánsson, A., Arnórsson, S., Gunnarsson, I., Kaasalainen, H., and Gunnlaugsson, E. (2011) The geochemistry and sequestration of H₂S into the geothermal system at Hellisheidi, Iceland. *Journal of Volcanology and Geothermal Research*, 202, 179–188.
- Thiel, J., Byrne, J.M., Kappler, A., Schink, B., and Pester, M. (2019) Pyrite formation from FeS and H₂S is mediated through microbial redox activity. *Proceedings of the National Academy of Sciences*, 116, 6897–6902.
- Titschack, J., Baum, D., Matsuyama, K., Boos, K., Färber, C., Kahl, W.A., Ehrig, K., Meinel, D., Soriano, C., and Stock, S.R. (2018) Ambient occlusion—A powerful algorithm to segment shell and skeletal intrapores in computed tomography data. *Computers & Geosciences*, 115, 75–87.
- Toplis, M.J. (2005) The thermodynamics of iron and magnesium partitioning between olivine and liquid: criteria for assessing and predicting equilibrium in natural and experimental systems. *Contributions to Mineralogy and Petrology*, 149, 22–39.
- Vigliaturo, R., Marengo, A., Bittarello, E., Pérez-Rodríguez, I., Dražič, G., and Gieré, R. (2020) Micro- and nano-scale mineralogical characterization of Fe(II)-oxidizing bacterial stalks. *Geobiology*, 18, 606–618.
- Vogt, H., Chattopadhyay, T., and Stolz, H.J. (1983) Complete first-order Raman spectra of the pyrite structure compounds FeS₂, MnS₂ AND SiP₂. *Journal of Physics and Chemistry of Solids*, 44, 869–873.
- Welch, S.A., and Banfield, J.F. (2002) Modification of olivine surface morphology and reactivity by microbial activity during chemical weathering. *Geochimica et Cosmochimica Acta*, 66, 213–221.
- Welsch, B., Faure, F., Famin, V., Baronnet, A., and Bachelery, P. (2013) Dendritic crystallization: A single process for all the textures of olivine in basalts? *Journal of Petrology*, 54, 539–574.
- Wiggering, H., Neumann-Mahlkau, P., and Selbach, H.-J. (1992) Experimental procedures to simulate weathering under atmospheres which may have characterized the early Archean. In M. Schidlowski, S. Golubic, M.M. Kimberley, D.M. McKirdy, and P.A. Trudinger, Eds., *Early Organic Evolution: Implications for Mineral and Energy Resources*, p. 31–40. Springer.
- Wolery, T.J., and Jove-Colon, C.F. (2004) Qualification of Thermodynamic Data for Geochemical Modeling of Mineral-Water Interactions in Dilute Systems. United States. Department of Energy. Yucca Mountain Project Office.
- Xi, S., Zhang, X., Luan, Z., Du, Z., Li, L., Liang, Z., Lian, C., and Yan, J. (2019) Micro-Raman study of thermal transformations of sulfide and oxysalt minerals based on the heat induced by laser. *Minerals*, 9.
- Yao, X., Xia, F., Deditius, A.P., Brugger, J., Etschmann, B.E., Pearce, M.A., and Pring, A. (2020) The mechanism and kinetics of the transformation from marcasite to pyrite: In situ and ex situ experiments and geological implications. *Contributions to Mineralogy and Petrology*, 175, 27.
- Yao, X., Xia, F., Brugger, J., Kartal, M., and Adegoke, I.A. (2021) Rapid marcasite to pyrite transformation in acidic low-temperature hydrothermal fluids and saturation index control on FeS₂ precipitation dynamics and phase selection. *ACS Earth and Space Chemistry*, 5, 2453–2465.

MANUSCRIPT RECEIVED MARCH 15, 2021

MANUSCRIPT ACCEPTED AUGUST 26, 2021

MANUSCRIPT HANDLED BY LINDSAY J. MCHENRY

Endnote:

¹Deposit item AM-22-98057, Online Materials. Deposit items are free to all readers and found on the MSA website, via the specific issue's Table of Contents (go to http://www.minsocam.org/MSA/AmMin/TOC/2022/Sep2022_data/Sep2022_data.html).